Lithos 318–319 (2018) 494–508

Contents lists available at ScienceDirect

Lithos

journal homepage: www.elsevier.com/locate/lithos

Petrogenesis and tectonic setting of the Tuyeh-Darvar Granitoid (Northern Iran): Constraints from zircon U-Pb geochronology and Sr-Nd isotope geochemistry

Azin Naderi [a,*], Habibollah Ghasemi [a], José F. Santos [b], Fernando Rocha [b], William L. Griffin [c], Hadi Shafaii Moghadam [d], Lambrini Papadopoulou [e]

[a] Department of Petrology, Geochemistry and Economic Geology, Faculty of Earth Sciences, Shahrood University of Technology, 36199-95161 Shahrood, Iran
[b] Geobiotec, Departamento de Geociências, , Universidade de Aveiro, Portugal
[c] ARC center of Excellence for Core to Crust Fluid Systems, GEMOC ARC National Key Centre, Earth and Planetary Sciences, Faculty of Science and Engineering, Macquarie University, NSW 2109, Australia
[d] School of Earth Sciences, Damghan University, 36716-41167 Damghan, Iran
[e] Department of Mineralogy-Petrology-Economic Geology, School of Geology, AUTh, GR 54124 Thessaloniki, Greece

ARTICLE INFO

Article history:
Received 6 January 2018
Accepted 28 August 2018
Available online 1 September 2018

Keywords:
A-type granitoid
Zircon U-Pb
Sr-Nd isotopes
Carboniferous
N Iran

ABSTRACT

Tuyeh-Darvar granitoid, which outcrop *ca* 45 km Sw of Damghan city, in the Eastern Alborz zone, comprise mainly the pluton emplaced into the Barut Formation of Lower Cambrian ages. Zircon U-Pb ages show Carboniferous ages (325 ± 3 Ma) for the formation of this granitoid. The granitoid is mostly metaluminous, ferroan and alkalic monzonite to monzodiorite. "These rocks have high values of FeOT/MgO and Ga/Al, high concentrations of K2O+Na2O, low abundances of MgO and transitional elements. Plots normalized to chondrite and primitive mantle compositions show strong enrichments of LREE relative to HREE and of LILE relative to HFSE, accompannied by negative anomalies of Nb and Sr."They contain Fe-rich hydrous mafic minerals and magnetite. These features are typical of A-type granites. Sr-Nd isotopic geochemistry, with initial εNd values from −1.1 to −1.5 and initial $^{87}Sr/^{86}Sr$ ratios between 0.70562 and 0.70678, are consistent with magmatic differentiation from mafic melts produced from an enriched mantle source. However, other models such as melting of mafic crust or mixing of components from depleted mantle and continental crust cannot be discarded. On the basis of the U-Pb zircon age (325 ± 3 Ma) and the known magmatic tectonic regime in Iran during the Paleozoic, it is suggested that the pluton, formed in a rift environment related to extensional structures of the Alborz block in Early Carboniferous time.

1. Introduction

Granitoids are the most abundant plutonic rocks in the upper continental crust and their genesis is related to many different tectonic and geodynamic processes, providing insights into the growth and chemical evolution of the continental crust. Granitoids are commonly divided into I, S and M types according to mineral assemblages, petrography, geochemistry and isotopic characteristics (Barbarin, 1999; Chappell and White, 1974). Loiselle and Wones (1979) defined a fourth granitoid type, A-type (A stands for Anorogenic or Alkaline). The A-type granitoids are distinguished by high FeO_T/MgO, F/H_2O and Ga/Al ratios, and high contents of $K_2O + Na_2O$, high-field-strength elements (HFS) and trivalent rare earth elements (REE^{+3}) (e.g., Bonin, 2007, 2008). Mineralogically, they are characterized by Fe-rich hydrous mafic minerals (King et al., 1997).

Although the A-type granitoids are a relatively small part of the granitoid plutonism, the study of this category of granitoids has proved to contribute significantly to our understanding of post-collisional/intraplate extensional magmatic processes within the continental lithosphere (Bonin, 2007, 2008; Mushkin et al., 2003; Yang et al., 2006).

Eby (1990, 1992) subdivided A-type granitoids into A_1 and A_2 chemical subgroups. The first group (A_1) is characterized by geochemical features (such as Nb/Y ratio) similar to those found in oceanic-island basalts, while the second group (A_2) is characterized by features more similar to signatures of continental crust. These two types have been related to different tectonic situations: intra-continental rifting, for A_1-subtype; post-collisional setting, for A_2-subtype. However, Bonin (2007) stresses that there are transitional compositions between the two subtypes.

A-type granites of the Carboniferous–Permian time occur in the Eastern Pontides–Lesser Caucasus and NW Iran (Rolland et al., 2011; Shafaii Moghadam et al., 2015) and they are interpreted as testifying

* Corresponding author.
E-mail address: naderiazar@yahoo.com (A. Naderi).

https://doi.org/10.1016/j.lithos.2018.08.034
0024-4937/

for extensional tectonics related to the early stages of Neotethys opening.

The Tuyeh-Darvar granitoid, which is studied in the present work, is good representative of Carboniferous igneous activity in northern Iran.

The Tuyeh – Darvar granitoid pluton - with geographical coordinates from 53°50′ to 53°53′ E, in longitude, and 36° 01′ to 36° 03′ N, in latitude - is located north of tuyeh village 45 km SW of Damghan city in Semnan province, northern Iran). According to the structural geological division of Iran presented by Stöcklin (1968), this area belongs to the Alborz zone (Fig. 1). Four geological aspects (tectonic, sedimentary petrology, paleontology and economic geology) of the area have been focussed in previous works (e.g., Alavi, 1996), but, until now, the only petrological study on the Tuyeh-Darvar granitoid pluton is that of Khanalizadeh (2005), who has already considered it as an A-type granite. Since there was no detailed geochemical study, and especially no isotopic data, on this granitoid, this article presents new geochemical and isotopic (U-Pb dating, and Sr and Nd isotope geochemistry) results. With these data, it will be possible to discuss the petrogenesis and tectonic setting of the granitoid pluton on firmer grounds.

2. Geological background

Iran constructed from several structural units, which record the fragmentation of the northern Gondwana supercontinent in upper Paleozoic time (e.g., Stöcklin, 1968; Alavi, 2004, 2007; Shafaii Moghadam et al., 2017). The consequences of this fragmentation (divergent movements) and re-amalgamation and re-configuration (convergent movements) have been recorded as magmatic, metamorphic and sedimentary complexes in different structural zones.

The Alborz structural zone is one of the most important zones for following the geodynamic evolution of the Paleotethys Ocean. This zone extends in a sinuous E-W trending belt (2000 km in length) across northern

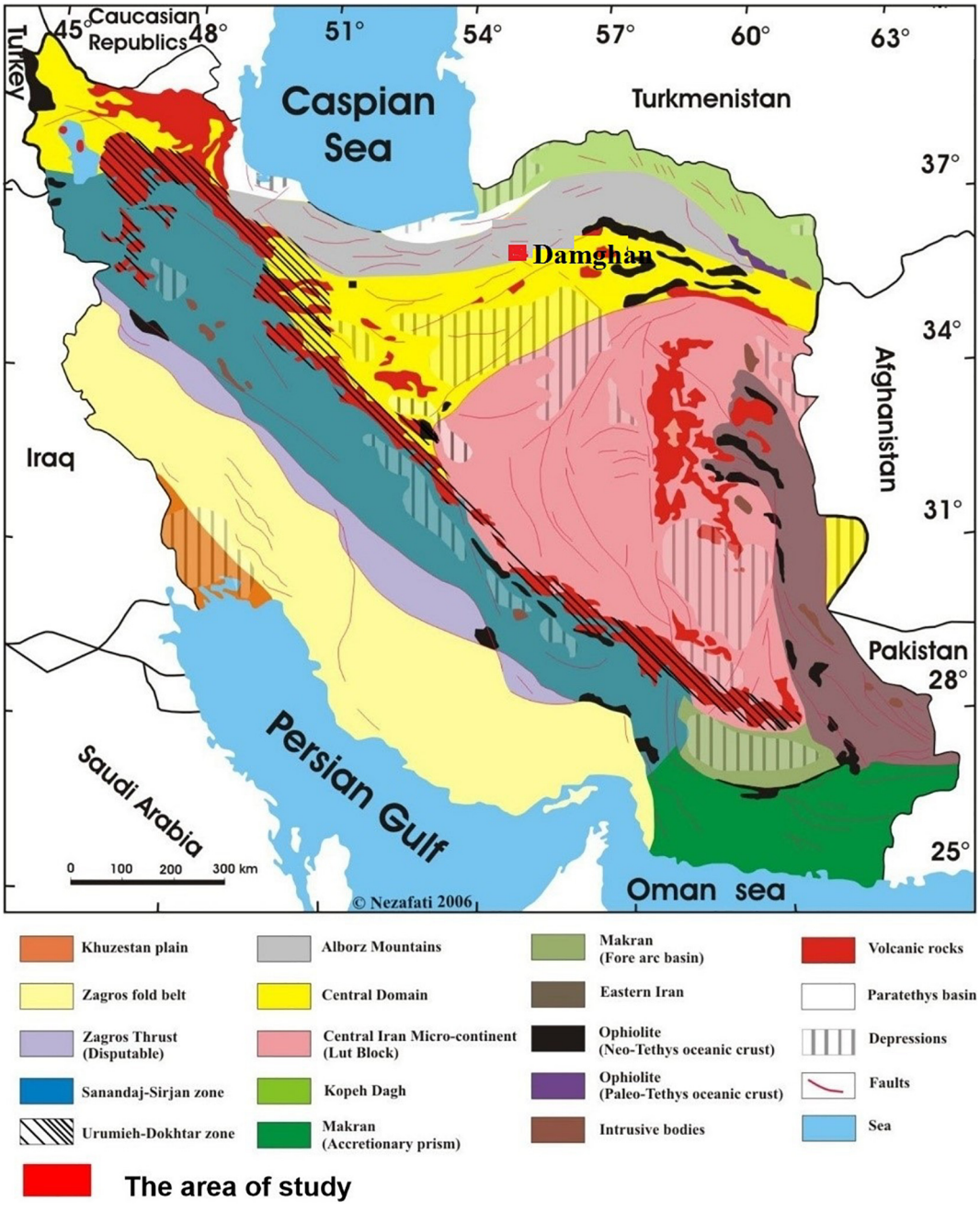

Fig. 1. The Structural zones of Iran; the study area is shown by a rectangle. (Modified from Stöcklin, 1968 (Nezafati, 2015).)

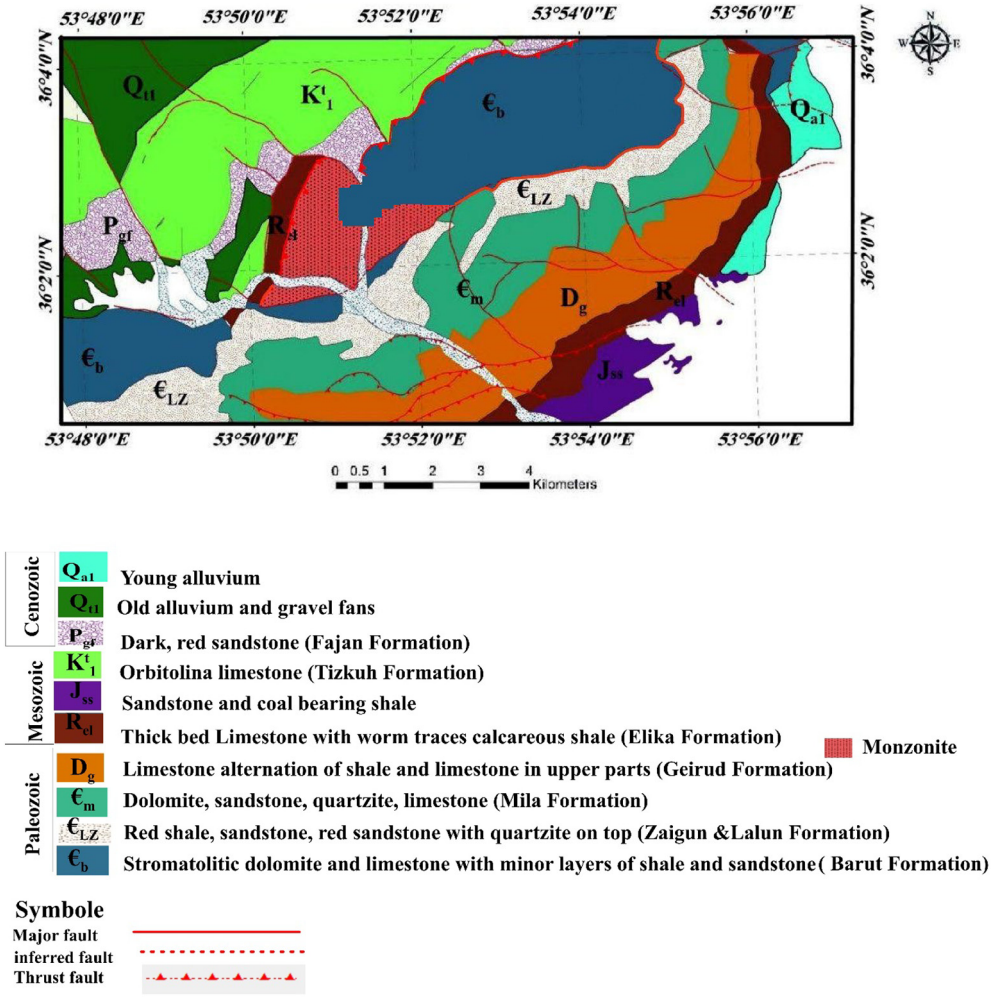

Fig. 2. Geological map of the Tuyeh – Darvar area.

Iran, parallel to the southern margin of the Caspian Sea, and consists of Phanerozoic magmatic, metamorphic, and sedimentary rocks. The Alborz zone was a part of the Gondwana plate in the early Paleozoic; it separated from Gondwana between the Ordovician and the Silurian and then collided with the Eurasian plate in Triassic time, causing the closure of the Paleo-Tethys Ocean in the north, and formation of the Neo-Tethys Ocean in the south (Muttoni et al., 2009). Paleozoic and early Mesozoic regional extensional events in Alborz block have been recognized by many researchers (Berberian and King, 1981; Derakhshi et al., 2017; Zanchi et al., 2006).

In Eastern and Central Alborz, extensional movements started in the Ordovician (Alavi, 1996; Derakhshi et al., 2017) and extended into the Devonian (Derakhshi et al., 2017). These extensional phases resulted in some regional rift basins with extensive magmatic activity (Berberian, 1983; Derakhshi et al., 2017). Extension, lithospheric rupture, ascent of mantle plumes and partial melting caused the development of the rift systems in Eastern and Central Alborz (Alavi, 1996; Derakhshi et al., 2017).

Despite the presence of large volumes of magmatic rocks, there unfortunately is little precise and accurate geochronology for magmatic and metamorphic events in this zone. Therefore, we do not have a clear understanding of the geodynamic processes that dominated the Paleozoic, Mesozoic and Cenozoic geological history of Alborz. Fortunately, in the recent years, some detailed studies have begun to focus on magmatic events in this zone (e.g., Alavi, 1996; Derakhshi et al., 2017). Now, we can discuss a regional geodynamic model on evolution of Alborz, which surely will improve as more detailed analyses of these magmatic rocks become available.

The Eastern Alborz is mainly comprised of Paleozoic and Mesozoic sedimentary sequences. The only magmatic sequence in this zone is Soltan Maydan Basaltic Complex (SMBC) with Upper Ordovician-Lower Silurian age (Derakhshi et al., 2017). Also, sporadic extrusive and intrusive magmatic rocks found in Ordovician, Devonian, Jurassic and Eocene.

The Tuyeh- Darvar granitoid occurs as a dome and covers an area of about 30 km^2. The pluton was emplaced into the Cambrian limestones and dolomitic limestones of the Barut formation (Fig. 2).

3. Petrography

According to petrographic studies, this granitoid can be classified as monzonite. Mineralogically, the granitoid consists mainly of plagioclase and orthoclase, accompanied by minor amounts of quartz, hornblende and biotite. Accessory minerals include magnetite, zircon, apatite, titanite and pyrite. Sericite, epidote, calcite, and chlorite are presented as secondary phases. This granitoid shows dominantly granular subhedral and porphyritic textures, but intergrowth textures, such as graphic and myrmekitic, are also observed. Plagioclase is the most abundant mineral; the plagioclase content is, in general, 40–60 vol%; it is tabular, euhedral to subhedral, and ranges from 0.1 mm to 1 cm; it is found commonly altered to sericite and saussurite. Alkali feldspar, which proportion ranges between 35 and 50 vol%, has tabular habit and euhedral to subhedral shapes, and its size varies from 2 to 50 mm in length, with the larger grains corresponding to phenocrysts. In seven samples, there are lamellae or patches of Na-rich feldspar hosted by orthoclase, forming a perthitic texture. Usually, the alkali feldspar shows evidence of

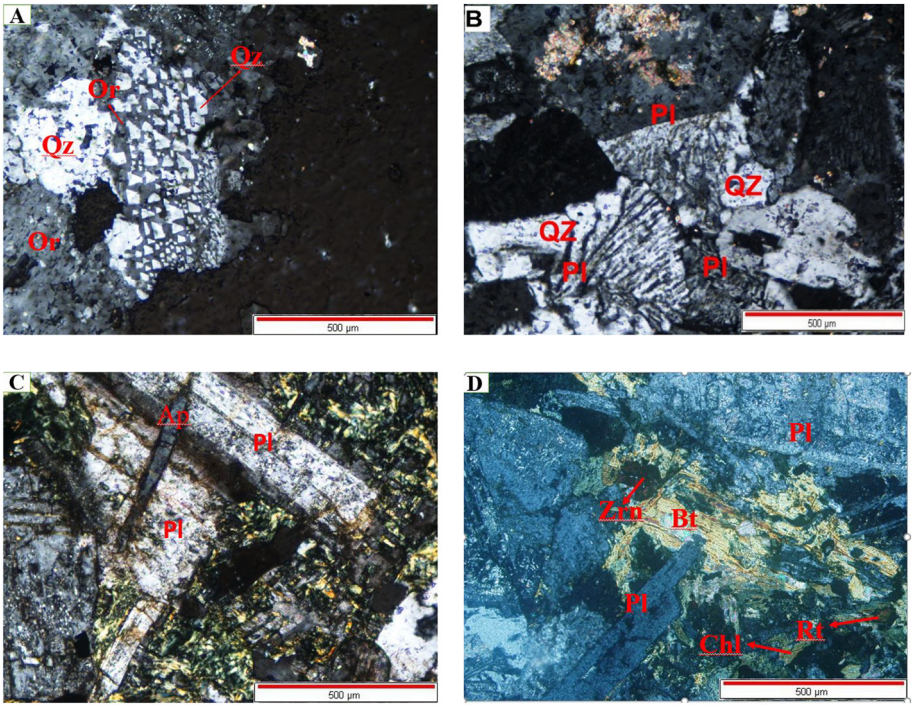

Fig. 3. Microphotographs of the Tuyeh-Darvar Pluton. (A). Graphic (granophyric texture) intergrowth of quartz and K-feldspar (crossed polarized light, XPL). (B) Myrmekite texture (simple intergrowth of quartz and sodic plagioclase) (XPL). (C) The presence of acicular apatite in monzonite, (crossed polarized light, XPL). (D). Secondary minerals (evidence of hydrothermal alteration in the granitoid) (XPL).

kaolinitization and sericitization. Quartz occurs as anhedral grains and makes up ~ 3–7% of the rock. It is also found interstitially in quartz – feldspar intergrowths, forming both granophyric and myrmekitic textures (Figs. 3A and B).

Biotite and hornblende are the main ferromagnesian phases in the granitoid and constitute 3–5% of the rock volume. Biotite, which is often chloritized, is subhedral and varies in size from 3 mm to 8 mm. Hornblende is present as subhedral prisms and in five samples is altered to chlorite, calcite and epidote. Accessory minerals (magnetite, zircon, apatite, titanite and pyrite) occur both as discrete grains and as inclusions the most abundant phases. In three sections, apatite has an acicular shape (Fig. 3C). They are engulfed by larger grains of other minerals. Secondary minerals, namely chlorite, calcite, sericite and epidote are evidence of hydrothermal alteration in the granitoid (Fig. 3D).

4. Analytical techniques

4.1. Whole-rock analytical procedures

Seventeen samples were selected as representative for major- and-trace element analysis by X-Ray Fluorescence (XRF) Spectrometry) and Inductively Coupled Plasma Mass Spectrometry (ICP- MS). Major- and minor elements were analyzed by XRF using an AXIOS X-Ray Fluorescence (XRF) Spectrometer at the Department of Geosciences of the University of Aveiro (Portugal). The XRF samples were prepared as pressed powder pellets. The REE compositions of the samples were determined by Inductively Coupled Plasma Mass Spectrometry (ICP- MS) at the Department of Geosciences of the University of Brighton (England). The ICP samples were prepared as follows: 0.1 g of sample was digested in 3 ml of concentrated nitric acid (ultra-pure) for 3 h and then topped up to 10 ml with type 1 water (18 M-O). These were then diluted 1:10 with type 1 water for analysis. Standards were matrix-matched to the samples and the ICP was calibrated at 10, 50, 100,500 ppb. Whole rock compositions of the Tuyeh-Darvar rocks are reported in Table 1.

4.2. Electron microprobe

Electron microprobe analyses were carried out in the Scanning Microscope Laboratory, Department of Mineralogy-Petrology-Economic Geology, School of Geology (A.U.Th), Thessaloniki, Greece, using a Scanning Electron Microscope - SEM (JEOL JSM-840A, Tokyo, Japan) equipped with an Energy Dispersive Spectrometer - EDS (INCA 250, Oxford) with 20 kV accelerating voltage and 0.4 mA probe current. Pure Co was used as an optimization element. For SEM observations, the sample was coated with carbon – average thickness 200 Å – using a vacuum evaporator JEOL-4×. Backscattered electron images were taken in order to detect areas of different chemical compositions, since the brightness of the BSE image tends to increase with the mean atomic number of an area. Mineral composition of the Tuyeh-Darvar rocks are reported in Table 2.

4.3. Zircon U- Pb dating

Three samples were chosen and prepared for U- Pb age dating by laser ablation multi-collector inductively coupled plasma mass spectrometry (LA- ICP- MS) method in the Geochemical Analysis Unit at the Macquarie University, Australia. Zircon grains were embedded and polished to half size and cleaned in acid before LA-ICP-MS trace-element and U-Th- Pb isotopic data were acquired at the same time on the same spot.

Zircon U-Th-Pb measurements were made on 30 μm diameter domains of single grains, following the protocols of Jackson et al. (2004). Isotopic ratios and element concentrations were calculated using GLITTER (ver4; Griffin et al., 2008). Concordia ages and diagrams were obtained using isoplot EX (version 3.75–4.15), (Ludwig, 2012). The common lead was corrected using the method of Andersen (2002). The USGS standards (AGV-1, BCR-1 and BHVO-1) were used for calibration and the Temora and Mud Tank reference zircons were analyzed in each run to control accuracy. Zircon U-Pb data are presented in Table 3.

Table 1
Whole – rock geochemical data for the Tuyeh- Darvar granitoid.

Sample	AT3	AT7	AT12	AT14	AT18	AT19	AT21	AT25	AT26	AT27	AT28	AT38	AT39	AT43	AT52	AT109	AT111
SiO2 (Wt)%	55.9	55.6	55.8	56.3	55.9	55.9	55.3	52.8	52.6	55.2	56.4	54.7	55.0	55.4	54.3	53.7	54.5
TiO2	1.15	1.29	1.38	1.22	1.41	1.41	1.35	1.05	1.26	1.35	1.21	1.43	1.25	1.30	1.33	1.45	1.42
Al_2O_3	14.6	14.1	14.9	14.4	15.6	14.6	15.0	18.7	15.7	14.1	14.5	14.8	14.5	14.6	14.3	15.2	14.7
Fe2O3t	11.1	11.9	9.7	10.4	10.3	10.2	12.4	9.7	9.0	12.0	10.1	10.9	11.5	10.5	12.9	10.9	12.1
MnO	0.13	0.15	0.12	0.14	0.07	0.09	0.13	0.08	0.13	0.15	0.15	0.08	0.13	0.21	0.19	0.15	0.99
MgO	1.36	1.71	1.33	1.53	1.79	1.50	2.61	2.04	1.45	1.62	1.51	1.60	1.48	2.40	2.17	1.63	3.28
CaO	4.62	4.74	4.71	4.34	2.65	4.57	2.11	4.39	5.44	4.81	4.25	4.96	4.61	4.02	4.15	4.69	3.57
Na2O	2.93	2.36	4.08	2.57	3.44	3.10	3.28	3.77	2.23	2.35	2.58	3.60	2.66	2.80	2.69	2.49	2.79
K2O	3.91	3.85	3.23	4.68	5.17	4.25	4.11	2.99	4.83	3.94	5.29	3.76	4.09	4.64	3.90	4.33	3.71
P2O5	0.69	0.69	0.71	0.69	0.71	0.67	0.77	0.32	0.66	0.74	0.84	0.89	0.77	0.79	0.84	0.68	0.797
LOI	3.25	3.31	3.88	3.19	2.68	3.15	2.68	3.93	6.58	3.07	2.76	2.67	3.57	2.76	2.55	4.23	2.5
Total	99.6	99.7	99.7	99.5	99.6	99.5	99.7	99.7	99.8	99.4	99.5	99.4	99.5	99.4	99.2	99.4	99.4
Ba(ppm)	839	696	640	911	1050	1010	1080	447	610	822	1780	980	863	1160	1040	559	793
Rb	174	171	172	195	198	209	241	173	232	218	298	171	199	247	236	225	180
Sr	290	310	327	305	331	261	575	356	187	338	619	430	308	538	394	190	335
Zr	440	400	450	430	440	420	500	300	380	400	430	430	390	430	390	380	430
Nb	39.7	38.0	39.6	37.0	36.8	34.6	40.0	24.2	40.2	37.3	35.0	36.6	33.6	30.7	33.8	34.3	36
Co	10.8	11.5	8.7	10.8	8.5	10.7	9.7	12.8	5.4	9.9	11.6	8.9	8.0	8.2	13.8	8.8	8.3
Zn	200	200	60	160	100	70	100	110	70	190	260	150	140	670	160	140	180
Ag	0.17		0.16	0.163	0.16	0.166		0.154	0.162	0.172	0.16	0.161	0.175	0.167	0.17	0.161	0.165
Cs	1.4	2.3	1	2.7	1.2	18	3	2.5	2.1	2.4	1.8	3.6	2.4	1.08	1.9	1.22	2.76
Hf	9	11.1	9	8.9	9.2	8.7	9.8	8.6	9.7	9	9.5	9.8	9.2	10	7.9	7.9	4.8
Cr	37.5	22.6	31.3	39.2	40.8	46.6	26.9	25	32.1	35.2	30.5	37	35.6	38.5	43.0	58.9	46.5
Sn	5.5	4.9	3.4	4.4	5.7	ND	4.2	5.5	6.1	6.3	4.9	4.3	6.5	4.7	6.5	4.0	5.3
Th	12.9	11.8	11.9	14.8	12.5	11.3	12.2	9.2	12.0	11.8	13.3	13.0	11.5	11.6	10.6	10.8	12.4
U	3.9	4.6	4.1	4.0	3.9	4.2	5.1	5.0	3.1	3.6	5.3	4.4	4.1	4.0	3.2	3.5	3.6
V	57.5	60.6	50.1	61.6	79.6	69.8	69.1	107.7	64.6	58.4	63.6	86.2	53.0	80.2	86.4	76.2	80.6
Pb	17.4	9.7	6.9	9.6	10.8	10.4	13.1	7.6	6.8	10.2	37.8	12.8	6.9	97.5	8.1	7.6	16.4
Cu				30.3	42.5			0		0	39.3	0	45.3				0
Cs	4.2	3.22	2.4	5.1	4.2	4.9	6.8	7.9	7.8	2.2	2.9	5	5.1	5.3	4.8	5.6	4.9
Ga	23.6	22.6	23.7	22.6	23.8	22.0	24.9	24.4	22.5	22.2	22.9	23.8	22.2	23.0	23.5	22.0	23.4
Ni	6.8	6.1	8.4	4.9	12.4	12.9	10.2	16.0	4.8	7.9	8.5	9.4	8.8	11.5	13.9	12.5	13.1
Sc	8.10	7.06	7.14	7.51	4.11	5.97	5.97	8.50	9.89	7.46	4.82	4.17	7.18	7.04	9.19	4.80	4.71
Y	37	27	33	29	28	25	37	22	40	39	33	24	24	33	30	32	24
La	55	32	28	38	55	31	64	11	27	59	26	33	9	23	25	41	45
Ce	118	71	64	80	111	67	132	32	65	118	65	60	76	30	53	107	85.5
Pr	14.85	8.38	8.09	8.92	13.95	7.32	16.50	3.75	7.14	14.57	5.78	6.25	7.45	3.54	5.36	9.34	7.31
Nd	53	35	35	37	46	31	51	17	31	43	25	27	32	17	24	40	29
Sm	10.90	7.59	8.10	7.66	9.52	6.96	10.40	3.86	7.48	8.83	5.29	6.48	6.74	4.46	5.83	7.99	6.29
Eu	1.90	1.33	1.21	1.15	2.46	1.21	2.09	0.92	0.85	1.09	0.62	0.87	0.94	0.92	1.10	1.72	1.31
Gd	11.06	7.74	8.68	7.94	9.39	7.11	10.34	4.22	8.34	9.17	5.31	6.78	6.69	4.87	6.38	7.39	6.4
Tb	1.53	1.06	1.27	1.11	1.24	0.96	1.40	0.65	1.28	1.27	0.71	1.03	0.89	0.74	0.97	0.87	0.89
Dy	7.77	5.49	6.76	5.78	5.91	4.95	7.07	3.69	7.16	6.77	3.41	5.66	4.32	3.98	5.29	3.96	4.62
Ho	1.40	0.98	1.24	1.06	1.02	0.86	1.27	0.69	1.35	1.24	0.59	1.06	0.73	0.70	0.97	0.66	0.84
Er	3.74	2.62	3.29	2.78	2.50	2.21	3.29	1.96	3.74	3.35	1.51	2.87	1.81	1.83	2.64	1.67	2.23
Tm	0.46	0.30	0.40	0.33	0.27	0.25	0.36	0.24	0.47	0.40	0.17	0.35	0.19	0.22	0.32	0.17	0.26
Yb	2.72	1.80	2.40	2.00	1.55	1.39	1.99	1.52	2.93	2.34	0.91	2.00	1.06	1.31	1.89	0.95	1.6
Lu	0.372	0.242	0.318	0.261	0.193	0.183	0.247	0.203	0.395	0.305	0.113	0.259	0.131	0.169	0.244	0.111	0.211

ND: Not determined.

4.4. Sr - Nd isotopes

Strontium and neodymium isotope compositions were determined at the Laboratory of Isotope Geology of the University of Aveiro, Portugal. Five powdered samples were dissolved by HF/HNO_3 mixture at 150 °C, using a hotplate. After evaporation of the final solution, the samples were dissolved with HCl (6 N) and dried again. The elements to analyze were purified using conventional two-stage ion chromatography technique: (i) separation of Sr and REE in ion exchange columns with AG8 50 W Bio-Rad cation exchange resin; (ii) separation of Nd from others lanthanides in columns with Ln Resin (Eichrom Technologies). All the reagents were sub-boiling distilled, and the water was produced by a Milli-Q Element (Millipore) apparatus. Sr was loaded on a single Ta filament with H_3PO_4, while Nd was loaded on a Ta outer side filament, with HCl, in a triple filament arrangement. $^{87}Sr/^{86}Sr$ and $^{143}Nd/^{144}Nd$ isotopic ratios were determined using a multi-collector Thermal Ionization Mass Spectrometer (TIMS) VG Sector 54. Data were obtained at dynamic mode with peak measurements at 1-2 V for ^{88}Sr and 0,8–1,5 V for ^{144}Nd. Sr and Nd isotopic ratios were corrected for mass fractionation relative to $^{88}Sr/^{86}Sr = 0.1194$ and $^{146}Nd/^{144}Nd = 0.7219$. During the current study, the SRM-987 standard gave an average value of $^{87}Sr/^{86}Sr = 710{,}266 \pm 17$ ($N = 12$; conf. Lim. = 95%) and the JNdi-1 standard gave an average value of $^{143}Nd/^{144}Nd = 0.5121037 \pm 57$ ($N = 11$; conf. Lim. = 95%). Whole rock Sr-Nd isotope compositions of the Tuyeh-Darvar rocks are reported in Table 4.

5. Geochemistry

In the SiO_2 *vs* ($Na_2O + K_2O$) classification diagram of Middlemost (1994) the granitoid samples plot in the monzonite and monzodiorite fields (Fig. 4A Anhydrous), and they plot in the alkalic field on the $Na_2O + K_2O$-CaO versus SiO_2 diagram of Frost and Frost (2008) (Fig. 4B Anhydrous).

In the $FeO^*/FeO^* + MgO$ *vs* SiO2 discrimination diagram, the samples with high FeOt/MgO, plot in the ferroan (A-type) field (Fig. 4C Anhydrous; Frost et al., 2001). According to the A/CNK versus A/NK diagram after Shand (1943), the samples are metaluminous and to slightly peraluminous (Fig. 4D Anhydrous).

Chondrite-normalized rare earth-element patterns (chondrite values from Boynton, 1984) show strong enrichment in LREEs relative

Table 2
Representative electron microprobe analyses of biotite from the granitoid.

SiO_2	38.83	39.06	41.49	40.78	38.22	40.19	39.32	39.37	38.74	41.79	38.78	39.22	38.33	41.13	39.30	38.32
TiO_2	3.36	3.65	3.35	3.36	4.25	3.51	3.93	3.80	3.11	2.94	3.10	3.03	3.60	3.05	3.32	2.92
Al_2O_3	12.27	11.62	10.38	11.06	11.00	10.56	10.80	11.27	11.80	10.70	10.56	10.85	11.25	10.63	10.38	10.33
FeO	29.11	21.82	19.76	19.97	23.39	21.36	22.16	21.97	21.22	19.65	25.05	23.71	24.54	21.07	22.83	27.75
MnO	0.43	0.58	0.38	0.00	0.36	0.27	0.19	0.00	0.00	0.29	0.00	0.40	0.00	0.06	0.00	0.00
MgO	3.87	8.86	10.06	10.45	7.49	10.12	9.33	9.78	11.57	10.92	7.50	8.41	7.41	9.32	8.67	5.57
CaO	0.04	0.21	0.00	0.09	0.28	0.03	0.23	0.24	0.00	0.00	0.19	0.00	0.02	0.02	0.01	0.06
Na_2O	0.08	0.27	0.72	0.55	0.00	0.53	0.00	0.16	0.19	0.01	0.00	0.28	0.24	0.38	0.04	0.00
K_2O	8.81	7.72	9.02	9.27	8.70	9.29	8.78	9.02	8.55	9.08	8.86	8.59	8.71	9.66	9.37	7.61
Cr_2O_3	0.00	0.00	0.00	0.28	0.00	0.00	0.00	0.00	0.18	0.08	0.10	0.10	0.35	0.00	0.00	0.51
Cl	3.22	1.14	0.46	0.73	1.60	0.27	0.47	0.54	0.38	0.24	1.97	1.39	1.45	0.68	1.02	2.49
Total	97.80	94.92	95.62	96.53	95.28	96.13	95.21	96.15	95.75	95.70	96.10	95.98	95.89	95.99	94.94	95.54
O=Cl	0.73	0.26	0.10	0.16	0.36	0.06	0.11	0.12	0.09	0.05	0.44	0.31	0.33	0.15	0.23	0.56
O=F	0.00	0.00	0.00	0.00	0.00	0.00	0.00	0.00	0.00	0.00	0.00	0.00	0.00	0.00	0.00	0.00
Al	2.22	2.11	1.86	1.97	2.03	1.90	1.97	2.03	2.12	1.90	1.95	1.98	2.07	1.91	1.91	1.93
Si	5.96	6.03	6.29	6.15	5.98	6.13	6.07	6.02	5.91	6.30	6.07	6.08	5.98	6.27	6.14	6.09
Al_{IV}	2.04	1.97	1.71	1.85	2.02	1.87	1.93	1.98	2.09	1.70	1.93	1.92	2.02	1.73	1.86	1.91
Al_{VI}	0.18	0.15	0.15	0.11	0.01	0.03	0.04	0.05	0.03	0.20	0.01	0.06	0.05	0.18	0.05	0.03
Ti	0.39	0.42	0.38	0.38	0.50	0.40	0.46	0.44	0.36	0.33	0.36	0.35	0.42	0.35	0.39	0.35
Fe^{+3}	0.00	0.00	0.00	0.00	0.00	0.00	0.00	0.00	0.00	0.00	0.00	0.00	0.00	0.00	0.00	0.00
Fe^{+2}	3.74	2.82	2.51	2.52	3.06	2.73	2.86	2.81	2.71	2.48	3.28	3.07	3.20	2.69	2.98	3.69
Mn	0.06	0.08	0.05	0.00	0.05	0.03	0.02	0.00	0.00	0.04	0.00	0.05	0.00	0.01	0.00	0.00
Mg	0.89	2.04	2.27	2.35	1.75	2.30	2.15	2.23	2.63	2.45	1.75	1.94	1.72	2.12	2.02	1.32
Cr	0.00	0.00	0.00	0.03	0.00	0.00	0.00	0.00	0.02	0.01	0.01	0.01	0.04	0.00	0.00	0.06
Ni	0.00	0.00	0.00	0.00	0.00	0.00	0.00	0.00	0.00	0.00	0.00	0.00	0.00	0.00	0.00	0.00
Ca	0.01	0.03	0.00	0.01	0.05	0.00	0.04	0.04	0.00	0.00	0.03	0.00	0.00	0.00	0.00	0.01
Na	0.02	0.08	0.21	0.16	0.00	0.16	0.00	0.05	0.06	0.00	0.00	0.08	0.07	0.11	0.01	0.00
K	1.72	1.52	1.74	1.78	1.74	1.81	1.73	1.76	1.66	1.75	1.77	1.70	1.73	1.88	1.87	1.54
Fe/(Fe + Mg)	0.81	0.58	0.52	0.52	0.64	0.54	0.57	0.56	0.51	0.50	0.65	0.61	0.65	0.56	0.60	0.74

to HREEs (a characteristic feature of A- type granitoids (Alirezaei and Hassanzadeh, 2012; King et al., 1997), with high $(La/Lu)_N = 13–62$, $(Gd/Yb)_N = 2.3–4.8$, and negative Eu anomalies (Fig. 5A). Spider diagrams normalized to primitive mantle values from Sun and McDonough (1989) display negative anomalies in Ti, Nb, Sr and positive anomaly for Pb (Fig. 5B).

On the Th/Yb *vs* Nb/Yb diagram of Pearce (2008), the samples plot in the OIB field (Fig. 6A). They also plot in the enriched mantle field of Pearce (1983) (Fig. 6B).

6. Mineral chemistry

6.1. Biotite

Representative analyses of biotites from Tuyeh-Darvar are given in Table 2. Biotite composition is useful for describing the nature of granitic magmas (Abdel-Rahman, 1994; Sepahi et al., 2012). These analyses of biotite indicate compositions lying in the biotite (Rieder et al., 1999) (Fig. 7A) and Fe-biotite fields (Foster, 1960) (Fig. 7B). Based on the discrimination diagram using Mg *vs* Al (Nachit, 1985) and major oxides (FeO *vs* MgO) of biotite in igneous rocks, and the discrimination diagram of Abdel-Rahman (1994), these biotites plot in the alkaline field (Fig. 8A,B), consistent with the whole- rock analyses.

7. U- Pb geochronology

Analyses of the zircons obtained from three samples of the Tuyeh-Darvar granitoid are presented in Table 3. All data are plotted on Concordia diagrams in Fig.9. Zircons from a monzonite sample (No. AT33) are transparent and colorless, with oscillatory zoning indicative of magmatic growth. The zircons are euhedral with prismatic forms, with an average length of about 200-250 μm and length/width ratios between 2:1 and 3:1. Analysis of 26 spots yielded a weighted mean $^{206}Pb/^{238}U$ age of 328 ± 1.8 Ma (1σ analytical uncertainty; MSWD = 2.4) (Fig. 9A).

U- Pb data on zircons from the monzodiorite sample (No. AT27) are plotted in Fig. 9B. The analyzed zircons are subhedral to euhedral and some show prismatic forms. The length/width ratios are 1:1 to 1:3, and all of them are yellow. The analysis of twenty points shows a weighted mean $^{206}Pb/^{238}U$ age of 321.3 ± 2.8 Ma (1σ analytical uncertainties, MSWD = 2.2).

Analyzed zircons from monzonite sample (No. AT43) are euhedral and show prismatic forms. They are relatively large with an average length of 300-500 μm, length/width ratios are 1:2 to 1:4, and all of them are transparent and colorless. The $^{207}Pb/^{206}Pb$ ages of twelve individual zircon analyses (Fig. 9C) give a mean $^{206}Pb/^{238}U$ age of 326.4 ± 3.8 Ma (1σ analytical uncertainty, MSWD = 3.6). These results define an early Carboniferous time for the crystallization and final emplacement of this pluton.

8. Sr-Nd isotope geochemistry

The results of Rb-Sr, and Sm–Nd isotope analyses are presented in Table 4 and initial Sr and Nd isotopic compositions (calculated for an age of 327 Ma) are plotted in Fig. 10. The $^{87}Sr/^{86}Sr_{(327Ma)}$ ratios range from 0.70562 to 0.70678, whilst $^{143}Nd/^{144}Nd_{(327Ma)}$ vary between 0.51214 and 0.51216, corresponding to slightly negative $\varepsilon Nd_{(327Ma)}$ values (−1.1 to −1.5) (Table 4). Compared to compositions of mantle-derived magmas, the granitoid rocks plot in the fields of oceanic-islands and continental basalts,

9. Discussion

9.1. Role of assimilation and fractional crystallization (AFC)

Chondrite-normalized rare earth element patterns for the granitoid show negative Eu anomalies (0.32–0.78), which reflect plagioclase fractionation. Primitive mantle-normalized rare earth element patterns show negative anomalies in Ba, Sr, Nb, Ce and Nd. Plagioclase fractionation could also be responsible for the negative Sr anomalies.

The samples show strong enrichments in LREEs relative to HREEs, as is characteristic of A- type granitoids. A negative anomaly in Nb is an important general feature of the continental crust (Han et al., 1997), and its presence in the granitoid reflect crustal contamination during the magma emplacement. Another reason for negative Nb and Ti anomalies in the granitoid is related to the fractionation of ilmenite, rutile and

Table 3
LA-ICP-MS zircon U-Pb analyses of the Tuyeh- Darvar granitoid samples.

Analysis no.	Th (ppm)	U (ppm)	Th/U	RATIOS (common-Pb corrected)							
				$^{207}Pb/^{206}Pb$	±1 s	$^{207}Pb/^{235}U$	±1 s	$^{206}Pb/^{238}U$	±1 s	$^{208}Pb/^{232}Th$	±1 s
AT-33-01	180	315	0.57	0.05413	0.00142	0.399	0.010	0.05351	0.00049	0.01423	0.00040
AT-33-02	167	247	0.68	0.06519	0.00203	0.462	0.014	0.05135	0.00058	0.01305	0.00044
AT-33-03	297	307	0.97	0.05333	0.00114	0.387	0.008	0.05263	0.00040	0.01758	0.00050
AT-33-04	88	146	0.60	0.05314	0.00197	0.372	0.013	0.05084	0.00062	0.01695	0.00069
AT-33-05	135	204	0.66	0.05389	0.00103	0.399	0.007	0.05368	0.00037	0.01589	0.00036
AT-33-06	154	283	0.55	0.06315	0.00188	0.448	0.013	0.05147	0.00056	0.01349	0.00047
AT-33-07	146	191	0.76	0.05364	0.00108	0.387	0.007	0.05233	0.00038	0.01486	0.00036
AT-33-08	123	183	0.67	0.05860	0.00185	0.420	0.013	0.05205	0.00057	0.01741	0.00075
AT-33-09	140	166	0.85	0.05376	0.00177	0.393	0.012	0.05306	0.00059	0.01662	0.00071
AT-33-10	118	176	0.67	0.05439	0.00119	0.410	0.009	0.05465	0.00043	0.01718	0.00049
AT-33-11	101	125	0.81	0.05386	0.00149	0.395	0.010	0.05327	0.00050	0.01563	0.00052
AT-33-12	190	238	0.80	0.05479	0.00134	0.393	0.009	0.05208	0.00045	0.01517	0.00051
AT-33-13	141	224	0.63	0.05333	0.00105	0.385	0.007	0.05241	0.00038	0.01508	0.00042
AT-33-14	173	260	0.66	0.05489	0.00124	0.384	0.008	0.05073	0.00042	0.01486	0.00046
AT-33-15	133	198	0.67	0.05376	0.00133	0.381	0.009	0.05145	0.00045	0.01570	0.00054
AT33–16	154	231	0.67	0.05348	0.00165	0.377	0.011	0.05115	0.00054	0.01446	0.00043
AT33–17	121	189	0.64	0.05307	0.00118	0.380	0.008	0.05195	0.00040	0.01694	0.00041
AT33–18	142	233	0.61	0.05300	0.00123	0.383	0.008	0.05239	0.00043	0.01622	0.00041
AT33–19	185	283	0.66	0.05599	0.00173	0.403	0.012	0.05218	0.00057	0.01407	0.00047
AT33–20	113	155	0.73	0.05278	0.00128	0.365	0.008	0.05018	0.00041	0.01582	0.00039
AT33–21	159	242	0.65	0.05289	0.00134	0.373	0.009	0.05114	0.00045	0.01483	0.00040
AT33–22	151	221	0.68	0.05312	0.00106	0.389	0.007	0.05317	0.00038	0.01586	0.00038
AT33–23	53	242	0.22	0.18851	0.00310	13.471	0.208	0.51855	0.00362	0.14481	0.00532
AT33–24	122	1089	0.11	0.05966	0.00124	0.820	0.016	0.09970	0.00082	0.02767	0.00111
AT33–25	300	353	0.85	0.06486	0.00123	1.024	0.018	0.11463	0.00085	0.03628	0.00128
AT27–01	350	314	1.11	0.05322	0.00119	0.376	0.008	0.05130	0.00042	0.01551	0.00041
AT27–02	117	201	0.58	0.07077	0.00240	1.515	0.049	0.15533	0.00208	0.04071	0.00176
AT27–03	67	125	0.53	0.05542	0.00201	0.391	0.014	0.05122	0.00062	0.01755	0.00074
AT27–04	260	235	1.11	0.05676	0.00127	0.543	0.012	0.06939	0.00059	0.02100	0.00062
AT27–05	476	608	0.78	0.06080	0.00099	0.866	0.013	0.10339	0.00068	0.03306	0.00085
AT27–06	350	482	0.73	0.05472	0.00146	0.405	0.010	0.05376	0.00049	0.01724	0.00053
AT27–09	203	932	0.22	0.05533	0.00128	0.390	0.009	0.05108	0.00043	0.01379	0.00041
AT27–10	161	172	0.94	0.05399	0.00132	0.382	0.009	0.05132	0.00045	0.01514	0.00053
AT27–11	248	282	0.88	0.05604	0.00172	0.404	0.012	0.05229	0.00056	0.01663	0.00062
AT27–12	82	145	0.57	0.05541	0.00164	0.383	0.011	0.05011	0.00052	0.01527	0.00055
AT27–13	262	255	1.03	0.05765	0.00166	0.407	0.011	0.05124	0.00052	0.01239	0.00043
AT27–15	334	408	0.82	0.06518	0.00223	0.490	0.016	0.05460	0.00068	0.01989	0.00112
AT27–16	53	106	0.50	0.05409	0.00130	0.371	0.008	0.04975	0.00044	0.01393	0.00049
AT27–17	100	143	0.70	0.05406	0.00192	0.385	0.013	0.05168	0.00064	0.01336	0.00075
AT27–18	291	378	0.77	0.05322	0.00153	0.373	0.010	0.05086	0.00050	0.01665	0.00053
AT27–19	68	202	0.33	0.05375	0.00121	0.386	0.008	0.05202	0.00044	0.01470	0.00040
AT27–20	121	149	0.81	0.05357	0.00101	0.376	0.007	0.05091	0.00036	0.01516	0.00031
AT43–01	231	307	0.75	0.04764	0.00423	0.339	0.030	0.05159	0.00068	0.01638	0.00057
AT43–02	408	448	0.91	0.39984	0.07220	4.694	0.781	0.08514	0.00596	0.02179	0.01026
AT43–03	138	230	0.60	0.05566	0.00382	0.390	0.026	0.05087	0.00080	0.01585	0.00029
AT43–04	141	236	0.60	0.05781	0.00203	0.419	0.014	0.05261	0.00063	0.01700	0.00085
AT43–05	186	211	0.88	0.06456	0.00089	0.944	0.012	0.10607	0.00063	0.03318	0.00089
AT43–06	250	260	0.96	0.05323	0.00175	0.374	0.012	0.05089	0.00060	0.01332	0.00061
AT43–07	322	415	0.78	0.05481	0.00140	0.366	0.009	0.04849	0.00035	0.01513	0.00014
AT43–08	490	442	1.11	0.05443	0.00303	0.397	0.021	0.05302	0.00097	0.01699	0.00136
AT43–10	289	261	1.11	0.05859	0.00135	0.411	0.009	0.05084	0.00043	0.01508	0.00050
AT43–11	553	650	0.85	0.05354	0.00132	0.395	0.009	0.05358	0.00045	0.01734	0.00042
AT43–12	157	287	0.54	0.10670	0.00264	0.853	0.019	0.05797	0.00063	0.01779	0.00054

Analysis no.	AGES (common-Pb corrected, Ma)								Disc. %	Correction type
	$^{207}Pb/^{206}Pb$	±1 s	$^{207}Pb/^{235}U$	±1 s	$^{206}Pb/^{238}U$	±1 s	$^{208}Pb/^{232}Th$	±1 s		
AT-33-01	376	60	341	7	336	3	286	8	11.0	None
AT-33-02	780	67	385	9	323	4	262	9	60.1	None
AT-33-03	343	50	332	6	331	2	352	10	3.7	None
AT-33-04	335	86	321	10	320	4	340	14	4.7	None
AT-33-05	366	44	341	5	337	2	319	7	8.3	None
AT-33-06	713	65	376	9	324	3	271	9	56.0	None
AT-33-07	356	47	332	5	329	2	298	7	7.9	None
AT-33-08	552	71	356	9	327	3	349	15	41.9	None
AT-33-09	361	76	337	9	333	4	333	14	7.9	None
AT-33-10	387	50	349	6	343	3	344	10	11.8	None
AT-33-11	365	64	338	8	335	3	313	10	8.7	None
AT-33-12	404	56	337	7	327	3	304	10	19.5	None
AT-33-13	343	46	331	5	329	2	303	8	4.1	None
AT-33-14	408	52	330	6	319	3	298	9	22.3	None
AT-33-15	361	57	328	7	323	3	315	11	10.7	None
AT33-16	349	71	325	8	322	3	290	9	8.1	None
AT33-17	332	52	327	6	326	2	340	8	1.7	None

Table 3 (*continued*)

Analysis no.	AGES (common-Pb corrected, Ma)								Disc. %	Correction type
	$^{207}Pb/^{206}Pb$	±1 s	$^{207}Pb/^{235}U$	±1 s	$^{206}Pb/^{238}U$	±1 s	$^{208}Pb/^{232}Th$	±1 s		
AT33-18	329	54	329	6	329	3	325	8	-0.1	None
AT33-19	452	70	344	9	328	3	282	9	28.2	None
AT33-20	319	56	316	6	316	3	317	8	1.2	None
AT33-21	324	59	322	7	322	3	298	8	0.8	None
AT33-22	334	46	334	5	334	2	318	8	0.0	None
AT33-23	2729	28	2713	15	2693	15	2733	94	1.7	None
AT33-24	591	46	608	9	613	5	552	22	-3.8	None
AT33-25	770	41	716	9	700	5	720	25	9.7	None
AT27-01	338	52	324	6	322	3	311	8	4.8	None
AT27-02	951	71	937	20	931	12	807	34	2.3	None
AT27-03	429	83	335	10	322	4	352	15	25.7	None
AT27-04	482	51	440	8	432	4	420	12	10.7	None
AT27-05	632	36	634	7	634	4	657	17	-0.3	None
AT27-06	401	61	346	7	338	3	345	11	16.2	None
AT27-09	426	53	334	6	321	3	277	8	25.2	None
AT27-10	371	56	328	6	323	3	304	11	13.3	None
AT27-11	454	70	345	9	329	3	333	12	28.3	None
AT27-12	429	68	329	8	315	3	306	11	27.2	None
AT27-13	516	65	347	8	322	3	249	9	38.6	None
AT27-15	780	74	405	11	343	4	398	22	57.6	None
AT27-16	375	55	320	6	313	3	280	10	16.9	None
AT27-17	374	82	331	10	325	4	268	15	13.4	None
AT27-18	338	67	322	8	320	3	334	11	5.6	None
AT27-19	361	52	331	6	327	3	295	8	9.6	None
AT27-20	353	44	324	5	320	2	304	6	9.6	None
AT43-01	81	197	296	23	324	4	328	11	-306.7	Disc
AT43-02	3908	291	1766	139	527	35	436	203	89.8	Disc
AT43-03	439	157	335	19	320	5	318	6	27.8	Disc
AT43-04	523	79	355	10	331	4	341	17	37.7	None
AT43-05	760	30	675	6	650	4	660	17	15.3	None
AT43-06	339	76	322	9	320	4	267	12	5.6	None
AT43-07	404	58	317	7	305	2	304	3	25.1	Disc
AT43-08	389	128	339	15	333	6	341	27	15.0	None
AT43-10	552	51	349	6	320	3	303	10	43.1	None
AT43-11	352	57	338	7	336	3	347	8	4.5	None

titanite during the differentiation of the magma (Green, 1994; Han et al., 1997). Accessory minerals such as titanite, ilmenite, rutile, fluorapatite, allanite, monazite and zircon have an important role in controlling the contents of the HFSEs (i.e., Y, Ta, Nb, and Th), because the elements have high partition coefficients for these minerals. (e.g. Rollinson, 1993). Gromet and Silver (1983) indicated that allanite and titanite account for 80–95% of the REEs in some granitoids. Similarly, allanite, titanite, fluorapatite, zircon, monazite and Th-orthosilicates control the concentrations of REE, Y, Th, and U in metaluminous granites (Bea, 1996). Therefore, the removal of accessory minerals during partial melting or via crystal fractionation means the interpretation of trace element characteristics can be complicated (Whalen et al., 1996). Nevertheless, obvious enrichments in some LILE (such as Rb and Th) and HFSE (such as Zr, Y and REEs except Eu, and the negative anomalies of Ba and Sr relative to primitive mantle normalized plots, are features of A-type granitoids (Whalen et al., 1987; Wu et al., 2002). Depletions in Eu and Ti are evident in the multielement spider diagram (Fig. 5B) and in the REE pattern (Fig. 5A). Niobium and Ta are strongly compatible in rutile (Ta more than Nb) although their D values increase with increasing SiO_2 content (Foley et al., 2000). Sr is incompatible in titanite (Dsr ~ 0.2) and Dsr does not vary significantly with P, T, or composition of the melt (Green, 1994).

Ascent of the magma through continental crust could result in assimilation and fractional crystallization, and increase the Rb/K and LILE/HFSE ratios (Arjmandzadeh and Santos, 2014). However, the final fractionation of plagioclase leads to increasing Rb contents and dramatically decreasing Sr contents. As a result, the Rb/K ratios will increase with plagioclase fractionation (Han et al., 1997).

9.2. Petrogenesis

The initial $^{87}Sr/^{86}Sr$ isotopic values for the granitoid range from 0.70562 to 0.70678, calculated using the ^{87}Rb decay constant suggested by Villa et al. (2015). The granitoid shows a significant variation in the initial $^{87}Sr/^{86}Sr$ isotopic values compared to the more uniform Nd isotopes (Fig. 10), which is another characteristic of A- type granitoids (Han et al., 1997).

Table 4
Rb-Sr and Sm-Nd isotopic data for the granitoid pluton. Initial Sr isotopic compositions were calculated using ^{87}Rb decay constant suggested by Villa et al. (2015).

Sample	Sr (ppm)	Rb (ppm)	$^{87}Rb/^{86}Sr$	Error (2σ)	$^{87}Sr/^{86}Sr$	Error (2σ)	Nd (ppm)	Sm (ppm)	$^{147}Sm/^{144}Nd$	Error (2σ)	$^{143}Nd/^{144}Nd$	Error (2σ)	$^{87}Sr/^{86}Sr$ (327 Ma)	εNd (327 Ma)
AT 7	310	171	1.592	0.045	0.714066	0.000017	35.3	7.58	0.130	0.007	0.512417	0.000019	0.706775	−1.5
AT 14	305	196	1.858	0.053	0.714126	0.000027	36.7	7.65	0.126	0.007	0.512420	0.000012	0.705619	−1.3
AT 38	430	172	1.156	0.033	0.712066	0.000024	31.7	6.73	0.128	0.007	0.512425	0.000018	0.706771	−1.3
AT 52	394	236	1.734	0.049	0.713800	0.000024	26.2	6.13	0.141	0.008	0.512454	0.000015	0.705861	−1.3
AT 111	335	181	1.561	0.044	0.713066	0.000020	24.6	5.29	0.130	0.007	0.512438	0.000016	0.705916	−1.1

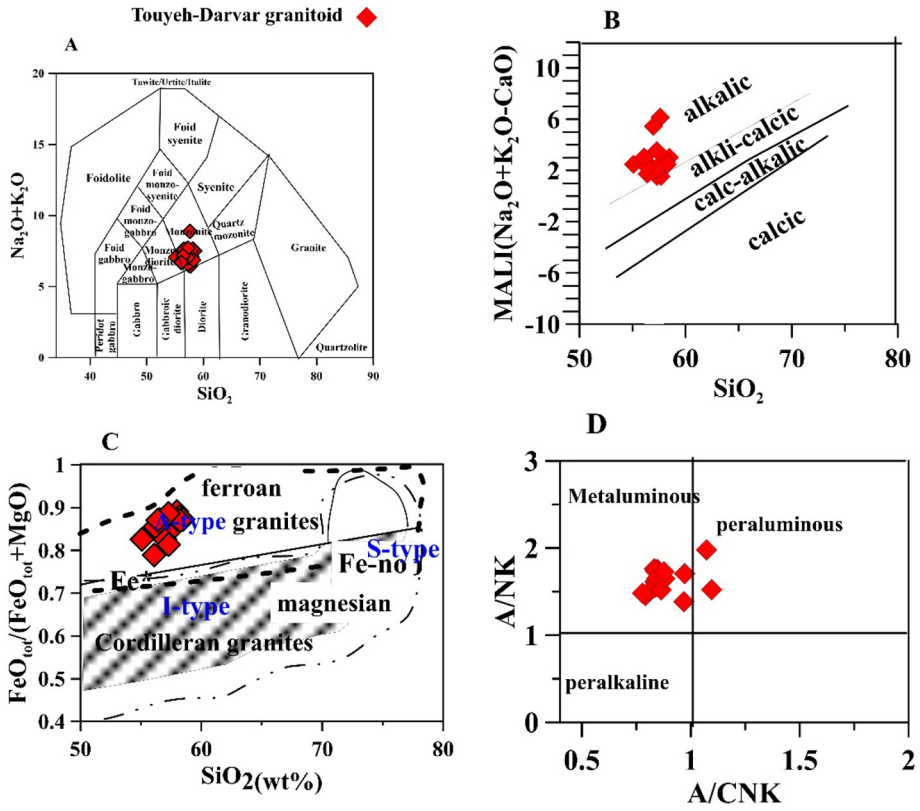

Fig. 4. Position of the granitoid samples in theclassification diagrams of A. Middlemost (1994); B. Frost and Frost (2008); Plotting of the granitoid samples in C. The FeO*/(FeO* + MgO) *vs* SiO_2 discrimination diagram (Frost and Frost, 2008), and D. The A/CNK *vs* A/NK diagram (Shand, 1943).

The Initial $^{143}Nd/^{144}Nd$ isotopic ratios for the granitoid are between 0.51214 and 0.51216. These values suggest a relationship between the Touyeh – Darvar granitoid and the enriched mantle (EM) (Fig. 10). EM components are characterized by low $^{143}Nd/^{144}Nd$ and variable $^{87}Sr/^{86}Sr$ (the low $^{87}Sr/^{86}Sr$ (EM I) and high $^{87}Sr/^{86}Sr$ (EM II)) (Zindler and Hart, 1986).

Therefore, in terms of their Sr and Nd isotopic ratios, the studied monzodiorite and monzonitecould result from magmatic differentiation of mafic melts produced in an enriched mantle source, as is documented in some extensional tectonic settings. As such, the Sr-Nd isotopic features are consistent with the elemental geochemical signatures that classify studied rocks as A-type granites (Fig. 10).

However, similar isotopic fingerprints could also result from melting of mafic crust which is resulting from previous emplacement and crystallization of basaltic magmas that produced in enriched mantle, or by mixing of components from depleted mantle and continental crust (through magma hybridization or by assimilation of crustal rocks by a mafic magma).

The slightly negative εNd (325 ± 3) from −1.11 to −1.51 and the slightly negative Nb anomalies in the studied samples can be reconciled by invoking crustal contamination. The Nb/La values for most samples are >0.5 (Nb/La = 0.53 to 1.10), which may indicate crustal contamination (Faure, 2013). This also is suggested by the following evidence: (1) depletions in HFSE (like Nb and Ti) relative to LILEs and LREEs suggest

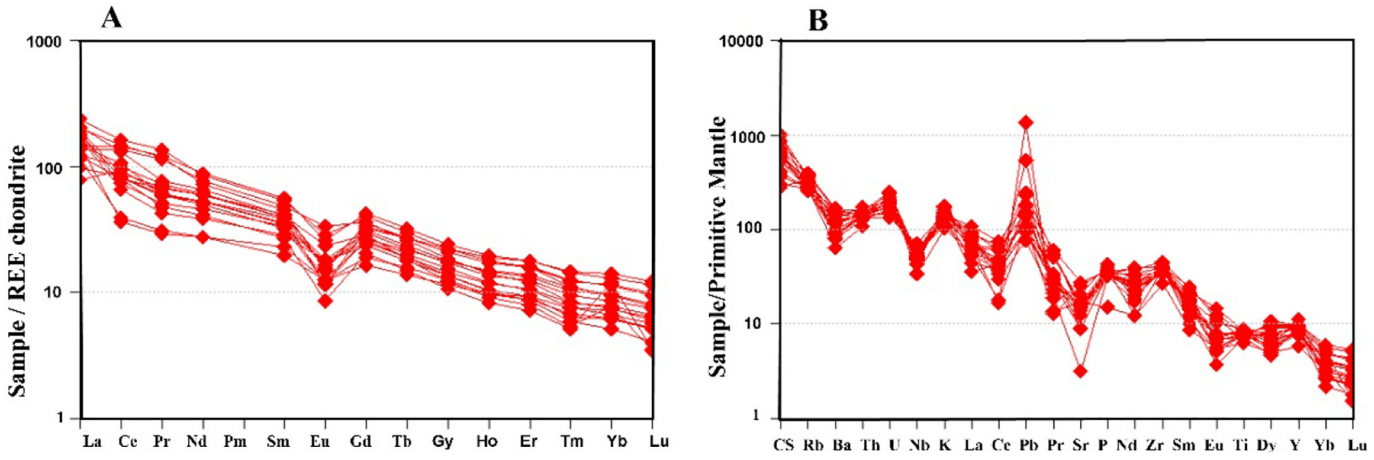

Fig. 5. A. Chondrite- normalized (values from Boynton, 1984) REE pattern and B. Primitive mantle–normalized (values from Sun and McDonough, 1989) spider diagram for granitoid samples.

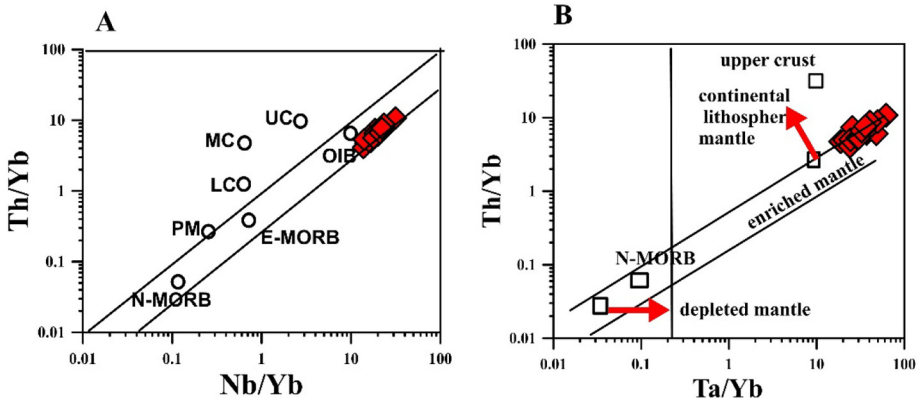

Fig. 6. Position of the granitoid samples in the A. Th/Yb *vs* Nb/Yb diagram (Pearce, 2008; Wang et al., 2016)). B. Th/Yb *vs* Ta/Yb diagram (Pearce, 1983). Values of N-MORB, E-MORB, OIB, and primordial mantle (PM) are from Sun and McDonough (1989); values of lower crust (LC), medium crust (MC) and upper crust (UC) are from Rudnick and Fountain (1995).

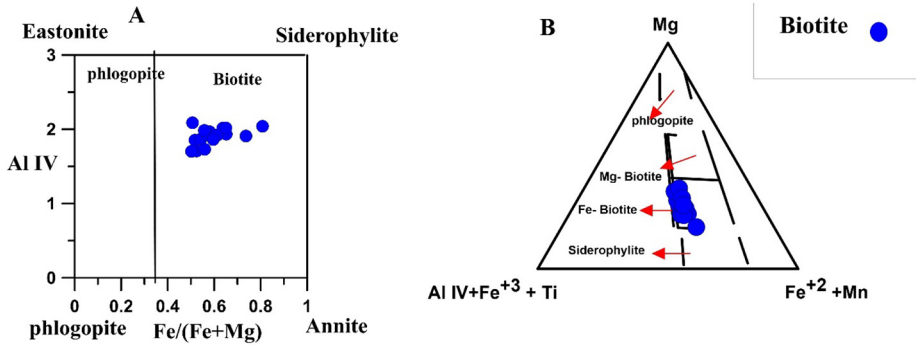

Fig. 7. Plotting of the granitoid biotites in the Classification diagrams for micas (modified after Rieder et al. (1999) and Foster (1960)).

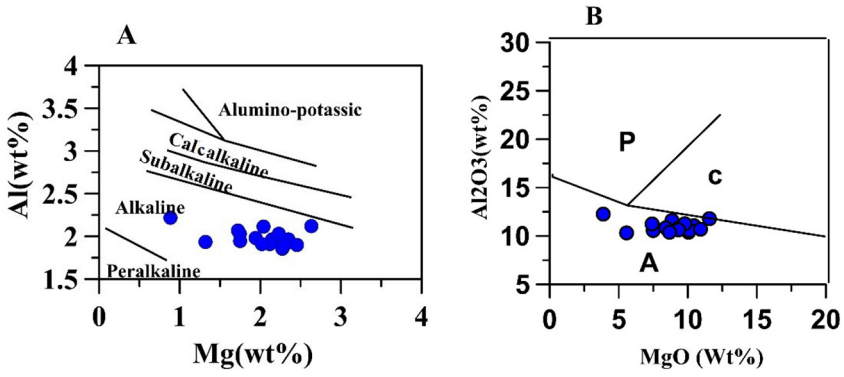

Fig. 8-. Plotting of the granitoid biotite compositions in the A. Mg *vs* Al diagram after Nachit (1985); (B) FeO* vs MgO Diagram (Abdel-Rahman, 1994). (Field A: anorogenic alkaline suites; Field P: peraluminous (including S-type) suites; Field C: calc-alkaline orogenic suites).

contamination by crustal materials during the ascent of the parental magma of the granitoid. (2) The Nb/Ta values, ranging from 0.47 to 0.77, suggest that the granitoid did not originate directly from a continental-crust source (cf. Eby, 2006). (3) The enrichment of samples in LREEs, Rb, K, Ba, Th and Cs and their low concentrations of transition elements like V and Sc could indicate an origin from an enriched mantle source beneath the continental lithosphere (Dargahi et al., 2010).

A type granites can have a broad range in Sr- Nd- Pb isotopic composition, which is often interpreted as the result of partial melting of distinct crustal and mantle- derived endmembers (Bonin, 1999; Dargahi et al., 2010).

In general, according to the geochemical and especially the isotopic data we can propose three petrogenetic models for Touyeh –Darvar granitoid:

1) In general, formation of A- type granitoids may occur in different geological settings with different ratios of crustal- and mantle-derived melts. The granitoid originated from depleted mantle that was metasomatized and enriched in LILE and REE prior to partial melting or the mafic magmas have undergone low degrees of fractional crystallization, and the residual liquids were emplaced and crystallized at upper crust as A- type granite.
2) The isotopic evidence is consistent with an enriched mantle source for the parental magma of the granitoid. In addition, some geochemical evidence, like depletion in Nb and Ti relative to LILE and LREE, suggests that the hypothesis of the occurrence of some crustal contamination can not be discarded."
3) Fractionation of mantle-derived mafic magmas with or without contribution of ancient crustal materials (c.f. Wu et al., 2002).

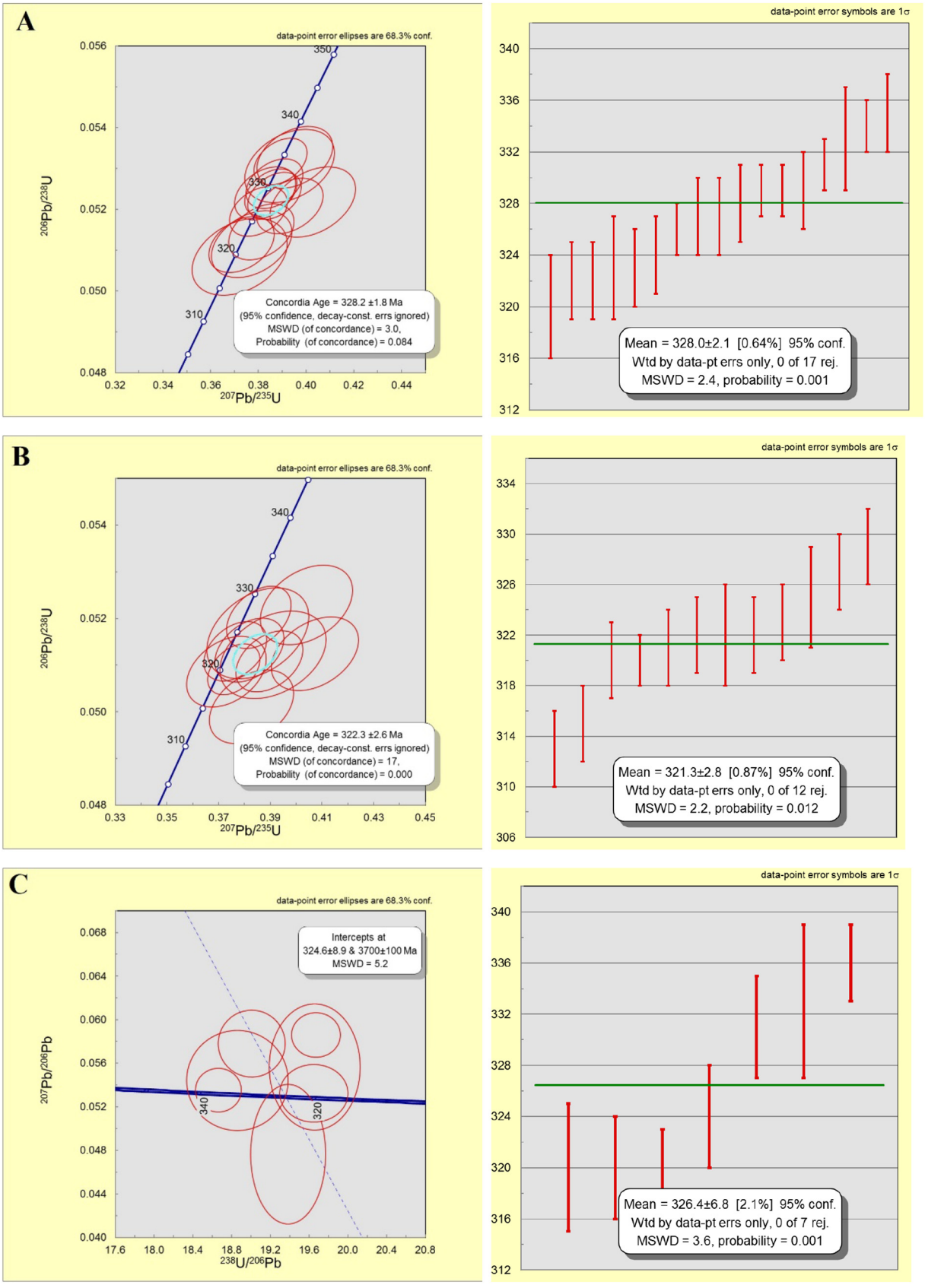

Fig. 9. Concordia diagrams for LA-ICP-MS zircon U-Pb data from the granitoid samples.

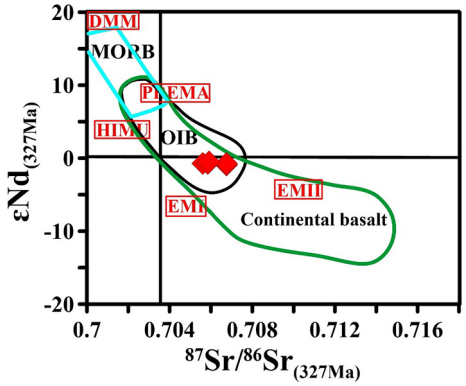

Fig. 10. Plot of $\varepsilon Nd_{(t)}$ *vs* $^{87}Sr/^{86}Sr_{(t)}$. Fields and reference compositions adapted from White (2015).

9.3. Tectonic setting

A-Type granites are distinguished from the other granites by several features: Al <0, (this index combines high ratios of FeO_t/MgO, Na2O + K2O, Na + K/Al, K/Na), high contents of Nb, Y, Zr, Zn, Ga, REE (excluding Eu), LILE, HFSE and low concentrations of Sr, Ba, CaO, MgO (Bonin, 2007; King et al., 1997). The petrographic, mineralogical, geochemical, and isotopic data, as well as discrimination diagrams of Nb and Zr *vs* 10000*Ga/Al (after Whalen et al., 1987) confirm that the Touyeh – Darvar granitoid is an A- type granitoid (Fig. 11).

In the geochemical discrimination diagrams of Eby (1992), the granitoid plots in the A_1 group, indicating derivation from the mantle (Fig. 12). The following characteristics also confirm that the studied pluton is an A_1 type granitoid: 1) In the Rb *vs* Y + Nb and Nb *vs* Y discrimination diagrams (from Pearce et al., 1984; Fig. 13A & B) all samples plot in the within – plate granite field (WPG). 2) The granitoid shows OIB – like signatures (Fig. 6A) similar to A_1 type granitoids. Biotite compositions for the pluton also plot in the anorogenic alkaline field in the tectonic-setting discriminant diagrams of Abdel-Rahman (1994)Fig. 14.

9.3.1. Tectonomagmatic model

In the tectonomagmatic regime prevailing in Iran during the Paleozoic, the granitoid ultimately formed owing to asthenospheric mantle, producing basaltic magmas in a rift environment related to extensional activity of the Alborz block in Early Carboniferous time.

Mantle-derived magmas intruded into rock units dating from Lower Cambrian (Barut formation) at shallow depths as intrusive (Fig. 15). According to Muttoni et al. (2009) Iran was located on the northern margin of Gondwana from Ordovician to Carboniferous time. Then, from the end of the Permian to the beginning of the Triassic, simultaneously with the opening of the Neo –Tethyan ocean between Iran and Arabia plates, Iran separated from Gondwana and eventually accreted to Laurasia (Stampfli and Borel, 2002). It appears that Iran moved 2500–3000 km to the north over 35 Ma (7-8 cm per year), (Alavi, 1996). Considering the ages of Tuyeh-Darvar rocks (325 ± 3 Ma) and the regional geology, mantle -related asthenosphere in Carboniferous time within the Gondwana, where Tuyeh- Darvar granitoid forms. We suggest the granitoid, formed due to the northward subduction of Alborz under Turan plate

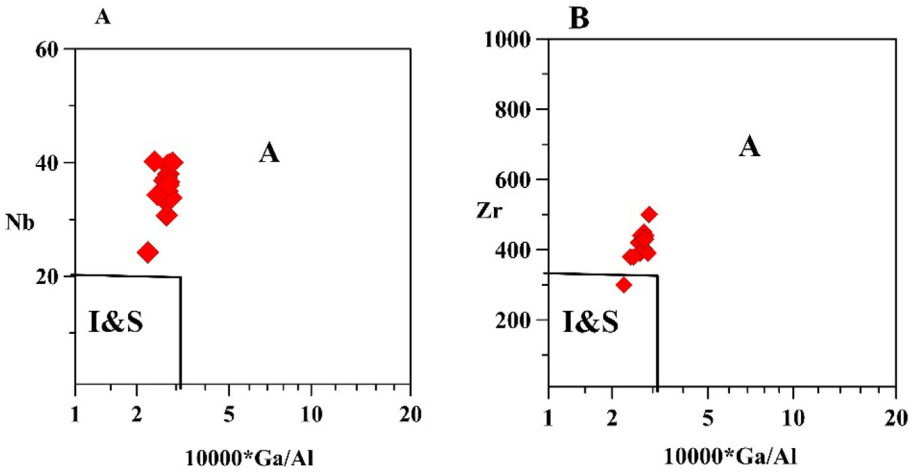

Fig. 11. Discrimination diagrams of Zr and Nb vs (10,000*Ga/Al) (From Whalen et al., 1987) for the granitoid.

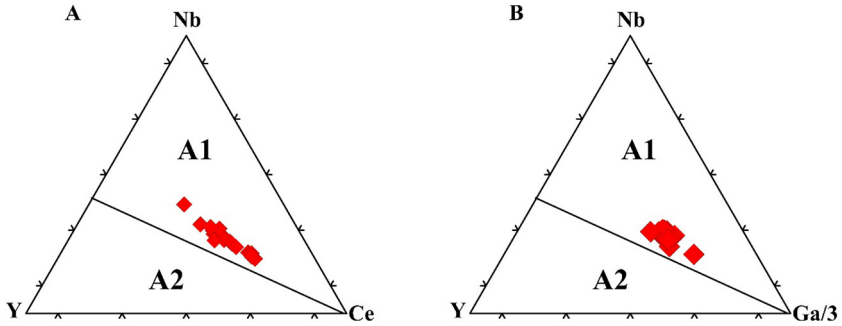

Fig. 12. Plots of discriminant diagrams of Nb-Y- Ce and Nb- Y-Ga (after Eby, 1992) for the granitoid.

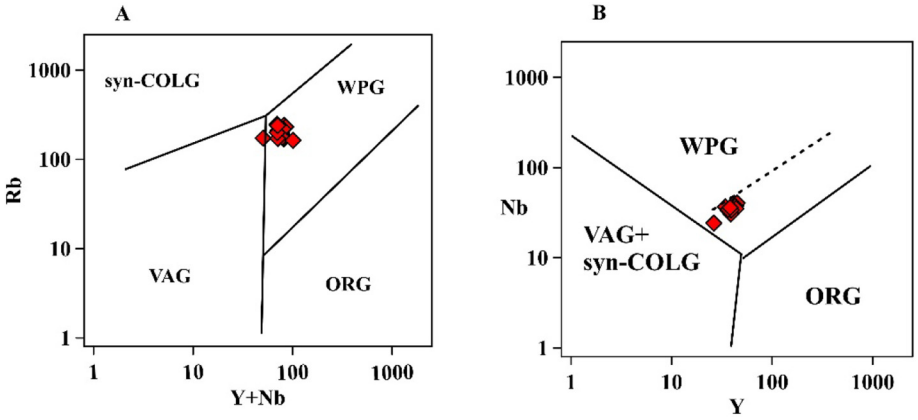

Fig. 13. A. Discrimination diagrams of (Y + Nb) versus Rb and Y versus Nb (From Pearce et al., 1984) for the granitoid.

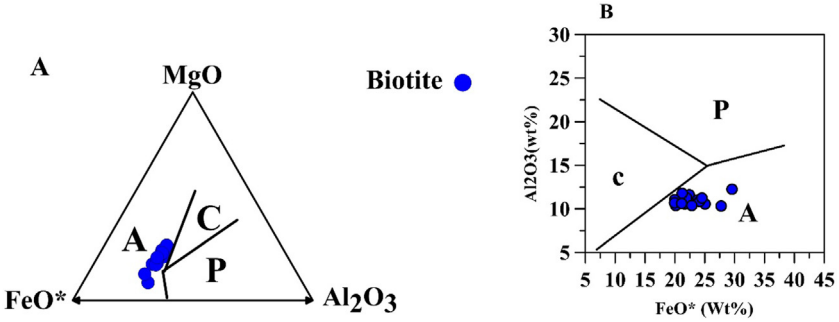

Fig. 14. Tectonic setting discriminant diagrams based on biotite composition for the Touyeh- Darvar pluton ((Field A: anorogenic alkaline suites; Field P: peraluminous (in-cluding S-type) suites; Field C: calc-alkaline orogenic suites), (Abdel-Rahman, 1994).

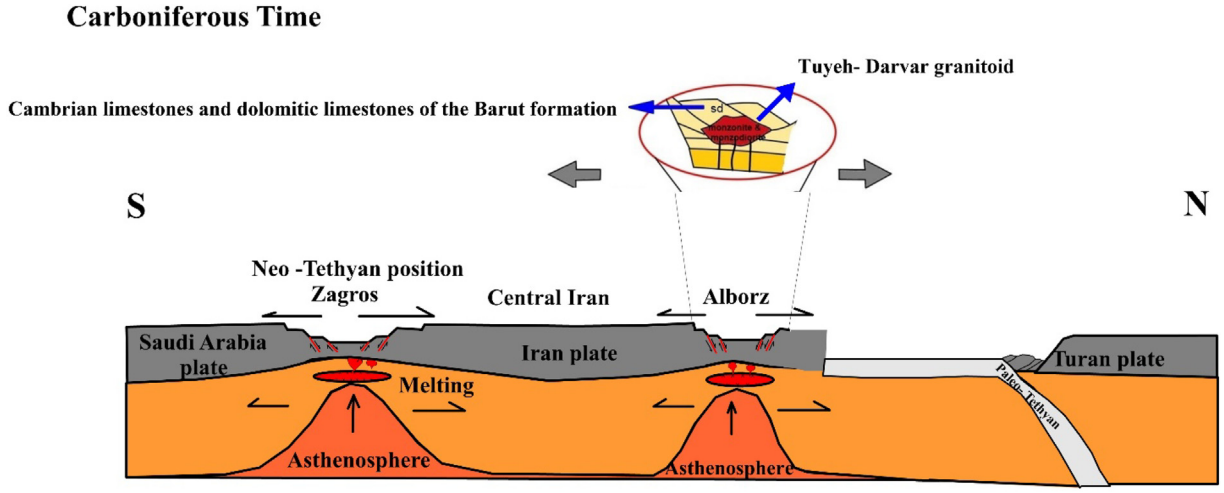

Fig. 15. Diagram illustrating the tectonic evolution of the Paleo-Tethys Ocean in Iran and tectonomagmatic model of the Touyeh- Darvar.

and fall of the oceanic slab into the mantle, in the south of subduction zone, Alborz continental slab was stretched and ruptured.

Then decreasing pressure on the mantle promoted its ascent and partial melting which resulted in adiabatic ascent of hot basic magma. This caused significant partial melting of the lower continental crust and formation of the granitoid melts. Following this process the basaltic magma differentiated and became contaminated with crustal magmas and produced granitoid magma.

Subsequently, the granitoid magma intruded into the rock units dating from Cambrian (Barut formation) at shallow depths.

Based on references that have been listed above (Tectonomagmatic model section) and our obtained data we reconstructed tectonic evolution of Paleo-Tethys in Gondwanaland during the Carboniferous in Iran (Fig. 15).

10. Conclusions

Field evidence shows that the Tuyeh-Darvar granitoid has intruded into the Cambrian limestone and dolomitic limestone of the Barut formation as a pluton. The granitoid has monzonite to monzodiorite

compositions and U-Pb zircon dating shows that the magmatism took place at around 325 ± 3 Ma, in the Lower Carboniferous.

According to the field observations, petrography, mineral chemistry, geochemistry and isotopic data, the granitoid is considered of A-type (A_1 subtype of Eby, 1992), suggesting that this intrusion is related to extensional structures in Alborz. The decrease of pressure on the mantle promoted its ascent. According to the magmatic tectonic regime in Iran during the Paleozoic time and on the basis of their U-Pb ages (325 ± 3 Ma), the granitoid formed due to extensional tectonics of the Alborz block. The northward subduction of Alborz under Turan plate and fall of the oceanic slab into the mantle, in the south of subduction zone, Alborz continental block was stretched and ruptured. Then decreasing pressure on the mantle promoted its ascent and partial melting which resulted in adiabatic ascent of hot basic magma. This caused significant partial melting of the lower continental crust and formation of the granitoid melts. Following this process the basaltic magma differentiated and became contaminated with crustal magmas and produced granitoid magma.

Subsequently, the granitoid magma intruded into the rock units dating from Cambrian (Barut formation) at shallow depths.

Acknowledgments

Authors wish to thank Mrs. Sara Ribeiro (Laboratory of Isotope Geology, University of Aveiro, Portugal) for TIMS analysis and for the guidance and assistance during sample preparation in the clean room. Dr. Mohammad Reza Naghizadeh is acknowledged for assistance during whole rock analysis at Brighton University (UK). The authors also would like to thank Cristina Sequeira for doing XRF analysis in University of Aveiro (Portugal). We also acknowledge Ministry of Science, Research and Technology of Iran and Vice Chancellor for Research in Shahrood University of Technology for supporting this research.

First author (AN) also wishes to express her sincere gratitude and appreciation to Prof. José F. Santos for his enormous help and support, for sharing his valuable knowledge and expertise, and providing a very warm and welcoming environment throughout her staying in Portugal. Special thanks go to the University of Aveiro (Portugal) for facilitating analytical analysis during her Sabbatical Leave year in Portugal. Part of this study (Zircon U- Pb dating) used instrumentation funded by ARC LIEF and DEST Systemic Infrastructure Grants, Macquarie University and industry. This is contribution 1205 from the ARC Centre of Excellence for Core to Crust Fluid Systems (www.ccfs.mq.edu.au) and 1254 from the GEMOC Key Centre (www.gemoc.mq.edu.au). We also thank Lambrini Papadopoulou, Assist. Professor, School of Geology, Aristotle University of Thessaloniki (Greece) for performing Microprobe analyses at the Scanning Microscope Laboratory of Aristotle University of Thessaloniki.

References

Abdel-Rahman, A.F.M., 1994. Nature of biotites from alkaline, calc-alkaline, and peraluminous magmas. J. Petrol. 35, 525–541.
Alavi, M., 1996. Tectonostratigraphic synthesis and structural style of the Alborz mountain system in northern Iran. J. Geodyn. 21, 1–33.
Alavi, M., 2004. Regional stratigraphy of the Zagros fold-thrust belt of Iran and its proforeland evolution. Am. J. Sci. 304, 1–20.
Alavi, M., 2007. Structures of the Zagros fold-thrust belt in Iran. Am. J. Sci. 307, 1064–1095.
Alirezaei, S., Hassanzadeh, J., 2012. Geochemistry and zircon geochronology of the Permian A-type Hasanrobat granite, Sanandaj–Sirjan belt: A new record of the Gondwana break-up in Iran. Lithos 151, 122–134.
Andersen, T., 2002. Correction of common lead in U-Pb analyses that do not report Pb-204. Chem. Geol. 192, 59–79.
Arjmandzadeh, R., Santos, J., 2014. Sr–Nd isotope geochemistry and tectonomagmatic setting of the Dehsalm Cu–Mo porphyry mineralizing intrusives from Lut Block, eastern Iran. Int. J. Earth Sci. 103, 123–140.
Barbarin, B., 1999. A review of the relationships between granitoid types, their origins and their geodynamic environments. Lithos 46, 605–626.
Bea, F., 1996. Residence of REE, Y, Th and U in granites and crustal protoliths; implications for the chemistry of crustal melts. J. Petrol. 37, 521–552.
Berberian, M., 1983. The southern Caspian: a compressional depression floored by a trapped, modified oceanic crust. Can. J. Earth Sci. 20, 163–183.
Berberian, M., King, G.C.P., 1981. Towards a palaeogeography and tectonic evolution of Iran. Can. J. Earth Sci. 18, 210–265.
Bonin, B., 1999. Alkaline rocks and geodynamics. Turk. J. Earth Sci. 7, 105–118.
Bonin, B., 2007. A-type granites and related rocks: evolution of a concept, problems and prospects. Lithos 97, 1–29.
Bonin, B., 2008. Death of super-continents and birth of oceans heralded by discrete A-type granite igneous events: the case of the Variscan–Alpine Europe. J. Geosci. 53, 237–252.
Boynton, W.V., 1984. Cosmochemistry of the rare earth elements: meteorite studies. Dev. Geochem. 2, 63–114.
Chappell, B.W., White, A.J.R., 1974. Two contrasting granite types. Pac. Geol. 8, 173–174.
Dargahi, S., Arvin, M., Pan, Y., Babaei, A., 2010. Petrogenesis of post-collisional A-type granitoids from the Urumieh–Dokhtar magmatic assemblage, Southwestern Kerman, Iran: constraints on the Arabian–Eurasian continental collision. Lithos 115, 190–204.
Derakhshi, M., Ghasemi, H., Miao, L., 2017. Geochemistry and petrogenesis of Soltan Maidan basalts (E Alborz, Iran): Implications for asthenosphere-lithosphere interaction and rifting along the N margin of Gondwana. Chem. Erde-Geochem. 77, 131–145.
Eby, G.N., 1990. The A-type granitoids: a review of their occurrence and chemical characteristics and speculations on their petrogenesis. Lithos 26, 115–134.
Eby, G.N., 1992. Chemical subdivision of the A-type granitoids, petrogenetic and tectonic implications. Geology 20, 641–644.
Eby, G.N., 2006. Distinctions between A-type granites and petrogenetic pathways. In: Dall'Agnol, R., et al. (Eds.), Symposium on Magmatism, Crustal Evolution, and Metallogenesis of the Amazonian Craton, Abstract Volume and Field Trips Guide. Belem, PRONEX-FPA/SBG-NO, p. 48.
Faure, G., 2013. Origin of Igneous Rocks: The Isotopic Evidence. Springer Science & Business Media, p. 115.
Foley, S.F., Barth, M.G., Jenner, G.A., 2000. Rutile/melt partition coefficients for trace elements and an assessment of the influence of rutile on the trace element characteristics of subduction zone magmas. Geochim. Cosmochim. Acta 64, 933–938.
Foster, M.D., 1960. Interpretation of the composition of trioctahedral micas. United States Geological Survey Professional Paper, 354-B, pp. 11–49.
Frost, B.R., Frost, C.D., 2008. A geochemical classification for feldspathic igneous rocks. J. Petrol. 49, 1955–1969.
Frost, B.R., Barnes, C.G., Collins, W.J., Arculus, R.J., Ellis, D.J., Frost, C.D., 2001. A geochemical classification for granitic rocks. J. Petrol. 42, 2033–2048.
Green, T.H., 1994. Experimental studies of trace-element partitioning applicable to igneous petrogenesis—Sedona 16 years later. Chem. Geol. 117, 1–36.
Griffin, W.L., Powell, W.J., Pearson, N.J., O'Reilly, S.Y., 2008. GLITTER: data reduction software for laser ablation ICP-MS. In: Sylvester, P. (Ed.), Laser Ablation-ICP-MS in the Earth Sciences: Current Practices and Outstanding Issues. vol. 40. Mineralogical Association of Canada Short Course, Vancouver, pp. 308–311.
Gromet, L.P., Silver, L.T., 1983. Rare earth element distributions among minerals in a granodiorite and their petrogenetic implications. Geochim. Cosmochim. Acta 47, 925–940.
Han, B.F., Wang, S.G., Jahn, B.M., Hong, D.W., Kagami, H., Sun, Y.L., 1997. Depleted-mantle source for the Ulungur River A-type granites from North Xinjiang, China: geochemistry and Nd–Sr isotopic evidence, and implications for Phanerozoic crustal growth. Chem. Geol. 138, 135–159.
Jackson, S.E., Pearson, N.J., Griffin, W.L., Belousova, E.A., 2004. The application of laser ablation-inductively coupled plasma-mass spectrometry to in situ U-Pb zircon geochronology. Chem. Geol. 211, 47–69.
Khanalizadeh, A., 2005. Geochemistry and Petrography of Tuyeh-Darvar intrusion, Southwest of Damghan. Shahrood University of Technology (M.Sc. Thesis, in Persian, abstract in English).
King, P.L., White, A.J.R., Chappell, B.W., Allen, C.M., 1997. Characterization and origin of aluminous A-type granites from the Lachlan Fold Belt, southeastern Australia. J. Petrol. 38, 371–391.
Loiselle, M.C., Wones, D.R., 1979. Characteristics and origin of anorogenic granites. Geol. Soc. Am. Abstr. Programs 11, 468.
Ludwig, K., 2012. User's Manual for Isoplot Version 3.75–4.15: A Geochronological Toolkit for Microsoft. Excel Berkley Geochronological Center Special Publication 5.
Middlemost, E.A., 1994. Naming materials in the magma/igneous rock system. Earth Sci. Rev. 37, 215–224.
Shafaii Moghadam, H., Li, X.H., Ling, X.X., Stern, R.J., Santos, J.F., Meinhold, G., Shahabi, S., 2015. Petrogenesis and tectonic implications of Late Carboniferous A-type granites and gabbronorites in NW Iran: Geochronological and geochemical constraints. Lithos 212, 266–279.
Moghadam, H.S., Li, X.H., Santos, J.F., Stern, R.J., Griffin, W.L., Ghorbani, G., Sarebani, N., 2017. Neoproterozoic magmatic flare-up along the N. margin of Gondwana: The Taknar complex, NE Iran. Earth Planet. Sci. Lett. 474, 83–96.
Mushkin, A., Navon, O., Halicz, L., Hartmann, G., Stein, M., 2003. The petrogenesis of A-type magmas from the Amram Massif, southern Israel. J. Petrol. 44, 815–832.
Muttoni, G., Mattei, M., Balini, M., Zanchi, A., Gaetani, M., Berra, F., 2009. The drift history of Iran from the Ordovician to the Triassic. Geol. Soc. Lond., Spec. Publ. 312, 7–29.
Nachit, H., 1985. Composition chimique des biotites et typologie magmatique des granitoids. C. R. Geosci. Paris 301, 813–818.
Nezafati, N., 2015. Mineral resources of Iran; an overview. 66 of Conference of Berg-und Hüttenmännischer Tag (BHT), At Freiberg, Germany 66, pp. 1–33.
Pearce, J.A., 1983. Role of the Sub-Continental Lithosphere in Magma Genesis at Active Continental Margins. Cheshire, Shiva Publications, Nantwich, pp. 230–249.
Pearce, J.A., 2008. Geochemical fingerprinting of oceanic basalts with applications to ophiolite classification and the search for Archean oceanic crust. Lithos 100, 14–48.

Pearce, J.A., Harris, N.B., Tindle, A.G., 1984. Trace element discrimination diagrams for the tectonic interpretation of granitic rocks. J. Petrol. 25, 956–983.
Rieder, M., Cavazzini, G., D'yakonov, Y.S., Frank-Kamenetskii, V.A., Gottardi, G., Guggenheim, S., Robert, J.L., 1999. Nomenclature of the micas. Mineral. Mag. 63, 267–296.
Rolland, Y., Sosson, M., Adamia, S., Sadradze, N., 2011. Prolonged Variscan to Alpine history of an active Eurasian margin (Georgia, Armenia) revealed by 40Ar/39Ar dating. Gondwana Res. 20, 798–815.
Rollinson, H., 1993. Using Geochemical Data: Evaluation, Presentation, Interpretation. Longman Group, UK (352 pp).
Rudnick, R.L., Fountain, D.M., 1995. Nature and composition of the continental crust: a lower crustal perspective. Rev. Geophys. 33, 267–309.
Sepahi, A.A., Maanijou, M., Salami, S., Gardideh, S., Khaksar, T., 2012. Mineral chemistry and geothermobarometry of Moshirabad pluton, Qorveh, Kurdistan, western Iran. Island Arc 21, 170–187.
Shand, S.J., 1943. Eruptive Rocks: Their Genesis, Composition, Classification, and Their Relation to Ore-Deposite. Wiley, New York (444p).
Stampfli, G.M., Borel, G., 2002. A plate tectonic model for the Paleozoic and Mesozoic constrained by dynamic plate boundaries and restored synthetic oceanic isochrons. Earth Planet. Sci. Lett. 196, 17–33.
Stöcklin, J., 1968. Structural history and tectonics of Iran: a review. Bull. Am. Assoc. Petrol. Geol. 52, 1229–1258.
Sun, S.S., McDonough, W.F., 1989. Chemical and Isotopic Systematics of Oceanic Basalts: Implications for Mantle Composition and Processes: Geological Society. Special Publications 42, London, pp. 313–345.
Villa, I.M., De Bièvre, P., Holden, N.E., Renne, P.R., 2015. IUPAC-IUGS recommendation on the half-life of 87 Rb. Geochim. Cosmochim. Acta 164, 382–385.
Wang, C., Chen, L., Bagas, L., Lu, Y., He, X., Lai, X., 2016. Characterization and origin of the Taishanmiao aluminous A-type granites: implications for Early Cretaceous lithospheric thinning at the southern margin of the North China Craton. Int. J. Earth Sci. 105, 1563–1589.
Whalen, J.B., Currie, K.L., Chappell, B.W., 1987. A-type granites: geochemical characteristics, discrimination and petrogenesis. Contrib. Mineral. Petrol. 95, 407–419.
Whalen, J.B., Jenner, G.A., Longstaffe, F.J., Robert, F., Gariepy, C., 1996. Geochemical and isotopic (O, Nd, Pb and Sr) constraints on A-type granite petrogenesis based on the Topsails Igneous Suite, Newfoundland Appalachians. J. Petrol. 37, 1463–1489.
White, W.M., 2015. Isotope Geochemistry. Wiley, Chichester (478 pp).
Wu, F.-y, Sun, D.-Y., Li, H., Jahn, B.-M., Wilde, S., 2002. A-type granites in northeastern China: age and geochemical constraints on their petrogenesis. Chem. Geol. 187, 143–173.
Yang, J.H., Wu, F.Y., Chung, S.L., Wilde, S.A., Chu, M.F., 2006. A hybrid origin for the Qianshan A-type granite, northeast China: geochemical and Sr–Nd–Hf isotopic evidence. Lithos 89, 89–106.
Zanchi, A., Berra, F., Mattei, M., Ghassemi, M.R., Sabouri, J., 2006. Inversion tectonics in central Alborz, Iran. J. Struct. Geol. 28, 2023–2037.
Zindler, A., Hart, S., 1986. Chemical geodynamics. Annu. Rev. Earth Planet. Sci. 14, 493–571.